A hybrid scheme for simulation of planar rigid bodies with impacts and friction using impact mappings

A hybrid scheme for simulation of planar rigid bodies with impacts and friction using impact mappings

Shane J. Burns*, Petri T. Piiroinen

School of Mathematics, Statistics & Applied Mathematics,
National University of Ireland, Galway,
University Road, Galway, Ireland

Abstract

This article introduces numerical techniques necessary for the implementation of impact maps derived from an energetic impact law for rigid-body impacts with friction at isolated contact points. In particular the work focuses on methodologies for long-term simulation with behaviours such as dynamic transitions and chatter. The methods are based on hybrid event-driven numerical solvers for ordinary differential equations together with system states to deal with the transitions. A slender rod impacting a periodically oscillating surface is used as an example to illustrate implementation and methods. The numerical scheme for the rod system is used to show how symmetry can play an important role in the presence of friction for long-term dynamics. This will show that surface oscillations with low frequencies tend to lead to periodic motions of the rod that are independent of friction. For higher frequencies however the periodic solutions are not that common and irregular motion ensues.

1. Introduction

Collisions or impacts in mechanical systems are very common and in many mechanical engineering applications they can cause undesired wear and noise and thus be very problematic and expensive. Two experimental examples of systems with such issues include an engine cam follower [32] and a magnetic bearing system [22].

In many applications energy is dissipated during impacts through motion in both the normal and tangential direction (friction) and how this happens has wide reaching effects on both the short-term and long-term dynamics. The understanding of the forces and impulses that occur at impact, together with an *impact law*, allows for some prediction of post-impact dynamics of impacting systems. By an impact law we mean a physical law that is based on theory and experimentation and used to describe the physics of a collision between bodies. Many impact law models have been developed, some of which include friction [7, 8, 11, 21, 28, 40, 18] and some which do not [9, 10]. Impact laws can be split into two main classes, those suitable for *compliant* rigid bodies ad those suitable for *non-compliant* rigid bodies. The first class of impact laws allows for deformation of the contacting regions of the bodies [5], whereas the second class of impact laws requires perfect rigidity together with some rigidity constraint [8].

The impact law used in this paper will be for non-compliant rigid-body impacts with friction. Typically, the main assumptions for non-compliant impacts are: (i) there is no deformation of the contact regions, (ii) an impact occurs at an isolated contact point, (iii) there is no moment impulse during impact, (iv) the contact duration is infinitesimal, (v) there is no change in generalised coordinates throughout the impact phase and (vi) the finite active forces can be neglected during impact, [8, 19].

The dynamics of rigid-body systems with impacts and friction is usually found by numerical integration of systems of ordinary differential equations (ODEs) corresponding to the mechanical system under question. There are two main schemes for how this is usually done, namely, *time-stepping* and *event-driven* schemes. How to choose one over the other depends on the class or type of mechanical system that is being analysed, how the impact law is resolved, and the type of numerical analysis one would like to perform. Time-stepping schemes consist of a time discretisation of the dynamics in which each time step is advanced by solving an appropriate *complementarity problem* [1]. In these schemes the moment of each collision or when changes in relative velocity between bodies occurs is not exactly located but instead some level of penetration can occur. This is the price to pay for using rigidly formulated time-stepping methods. These schemes are however very advantageous for the simulation of systems with a large number of degrees of freedom with multiple contacts, for example flows in a granular material or masonry structures. Event-driven schemes are also basically time-stepping schemes but the time for which a trajectory reaches a constraint or *discontinuity surface* is located as precisely as possible to avoid penetration. This

*Corresponding author. Tel: +353 91492332
Email addresses: shane.burns111@gmail.com (Shane J. Burns), petri.piiroinen@nuigalway.ie (Petri T. Piiroinen)

class of schemes can in turn be divided into two separate categories, the complementarity methods and the *hybrid* methods. As the name suggests, in the complementarity method a complementarity problem is solved as the event is located, whereafter the standard time-stepping scheme continues as discussed above [1].

In the hybrid methods, which are the focus of this paper, the integration is terminated when an event is located and a discrete map is applied to describe how the state changes at the event. When the map is applied the time-stepping scheme is restarted with the post-event states as the initial conditions with a new set of ODEs that reflect the new circumstance. Hybrid methods have some obvious drawbacks but also some very important advantages that we will use in this paper. The main complication of hybrid methods is that, since each event has to be identified and resolved individually, the complexity of all different combinations of events and ODEs grows very quickly with the number of possible events. Another complication is that for each event a mapping has to be found that reflects, in the case of this paper, what the impact law dictates. These issues make hybrid schemes only feasible for systems with relatively few different discontinuity surfaces [2, 35, 36]. However, on the positive side it is worth raising at least four different points. First, since the events are not included in the time stepping only ODEs with smooth dynamics have to be integrated and it is thus possible to use a suitable high-order integrator with well-known convergence properties so that trajectories can be found with high accuracy. Second, since no events will be lost during simulation hybrid methods are useful for the brute-force bifurcation analysis and in particular when *discontinuity-induced bifurcations* (DIBs) are involved. An example of a DIB, and something that will be seen in this article, is a *grazing bifurcation*. A grazing bifurcation occurs when, under parameter variation, a trajectory of a periodic orbit makes tangential contact with the discontinuity surface, resulting in a change in the system dynamics [30, 15]. Third, hybrid methods make the stability analysis of periodic orbits relatively straight forward since it is possible to calculate *saltation matrices* that "glue" fundamental solution matrices together for trajectories passing through regions between different events. Fourth, despite the common misconception, there are methods born out of hybrid schemes for impacting systems that can deal with the accumulation of impacts, sometimes referred to as *chatter* or *Zeno* behaviour, and also calculate the corresponding saltation matrices [31]. As mentioned above, event-driven schemes are particularly useful for systems with relatively few degrees of freedom, but with multiple spatially and temporally separated contact points. Some examples include turbine blade dampers, friction clutch vibrations, landing gear dynamics [33], passive walkers [2, 34] and braille printers [13].

The use of nonsmooth system theory to predict and understand the kinematics of colliding rigid bodies in the presence of impact and friction is a useful commodity in engineering in particular and research of such systems in general [6, 16, 22, 25, 33, 37]. It is well known that nonsmooth systems can exhibit complex behaviour that cannot be found in smooth systems. The class of systems with combinations of ODEs and maps, that we use here for mechanical systems with impact and/or friction, are often termed as *piecewise-smooth* (PWS) systems. In recent years the interest of DIBs found in PWS systems have increased dramatically, and as mentioned above the main driver of the analysis of DIBs have been the hybrid system approach, where local behaviour can numerically be pinpointed with high accuracy [3, 12, 15, 30, 31]. In particular DIBs in impacting systems without friction have been studied extensively and some classification methodologies have been developed in [14, 27, 24], but also impacting systems with friction have been studied from a DIB point of view [23, 17, 28]. As already mentioned, a type of behaviour that is very specific to impacting systems with rigid body impacts is chatter, which is the phenomenon whereby a system goes through an infinite number of impacts in a finite time period. Previous works on chatter have considered both frictionless systems [9, 12, 31] and systems with impacts and friction [23, 28, 29]. An interesting example of an engineering-based frictionless system is analysed in [26], where the problem of gear rattle (chatter) in Roots blower vacuum pumps is considered, and where the rattle is induced from the gear teeth losing and regaining contact. Similarly, in cam-follower systems for certain conditions the follower detaches from the cam, resulting in a series of unwanted impacts or chatter [3, 4, 32].

With this in mind, the emphasis of this paper is two-fold. First, we will show how the impact mappings for impacts with friction derived in [28] can be implemented for reliable simulations of systems with impacts and friction. Second, we want to exploit the fact that we have reliable simulation routines to analyse the long-term qualitative behavior of an unconstrained mechanical system with impacts and friction. Since previous research has mainly considered long-term dynamics for systems with impacts but without friction [3, 14, 31] the analysis of the unconstrained object will show that it is feasible to also consider long-term simulations for mechanical system with impact and friction. For this purpose we chose a hybrid event-driven technique as opposed to a time-stepping method in order to resolve DIBs in brute-force bifurcation analysis as well as deal with accumulation of events (chatter). We will use the example of a planar slender rod impacting with an oscillating surface to show how to implement these techniques. This can be seen as a generalisation of a system where a machine element detaches and is free to vibrate in the presence of friction or an item that lies on a vibrating conveyor belt. We will show how rattle is affected by the presence of friction.

This article is organised as follows. The equations of motion for a collision between two rigid bodies with an isolated contact point are derived in Section 2.2 along with an extension of the energetic impact law derived in [28] to allow for a two-body collision. Section 3 summarises the numerical methods necessary for the implementation of the chosen impact law. In Section 3.1 we will introduce the notion of system states and how this idea is used in the simulation of impacting systems. The model example of a slender rod impacting a periodically oscillating surface is introduced in Section 4 and the basic setup that is used in the numerical simulations is presented in Section 4.1. The paper concludes with a discussion in Section 5 that provides an insight for engineers and other researchers working with impact and friction.

2. Planar rigid-body impacts with friction

In this section we will derive a general framework for a planar rigid-body collision between two unconstrained objects. We will present an extension of the energetic impact mapping derived in [28], which will be used for the model example in Section 4. The extension derived here is more general than the mapping presented in [28] in that the mapping in [28] is for the specific case of a slender rod impacting a stationary non-compliant surface, but where we allow both bodies to be unconstrained.

2.1. Equations of motion

Consider two planar rigid bodies H and H' whose configuration relative to an inertial reference frame can be described in terms of vectors of generalized coordinates. Further impose that the bodies at any moment have a finite number of isolated contact points and contact can not occur at two separate points simultaneously. For this purpose we derive the equations of motion for two separate cases, when the bodies are in free flight, see Fig. 1 (a), and when they are in contact at an isolated point C, see Figs. 1 (b) and (c). The corresponding dynamics

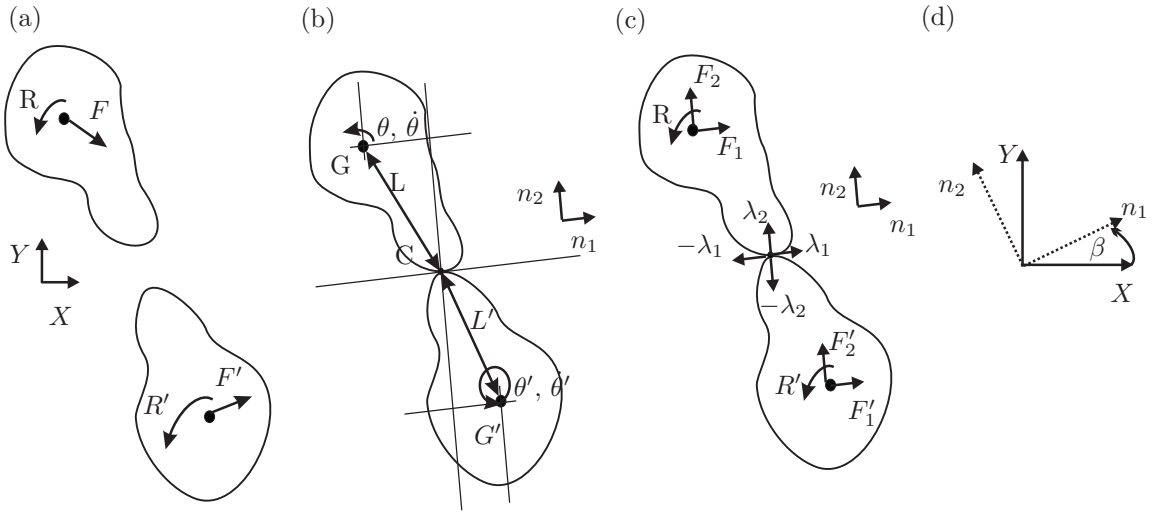

Figure 1: (a) A free-body force diagram for two planar bodies in free flight. (b) Geometry of two planar rigid bodies H and H' in contact at a point C. (c) A free-body force diagram corresponding to the figure in (b). (d)A schematic the showing angle of rotation β between the two frames used for modelling and analysis.

can be described using a Lagrangian formulation or using a Newtonian formulation. In Sections 2.1.1 and 2.1.2 we consider a Newtonian formulation.

2.1.1. Free flight

Consider the two bodies H and H' in free flight as shown in Fig. 1(a). The position and rotation of the centre of mass G of body H can be described in the $X-Y$ plane by the coordinates q_X and q_Y and the angle α, and similarly q'_X and q'_Y are the coordinates and α' the rotation of the centre of mass G' of body H' (see Fig. 1(a)). Next we let

$$r = (q_X, q_Y, \alpha)^T, \quad r' = (q'_X, q'_Y, \alpha')^T,$$
$$\dot{r} = (\dot{q}_X, \dot{q}_Y, \dot{\alpha})^T, \quad \dot{r}' = (\dot{q}'_X, \dot{q}'_Y, \dot{\alpha}')^T,$$

$$\ddot{r} = (\ddot{q}_X, \ddot{q}_Y, \ddot{\alpha})^T \quad \text{and} \quad \ddot{r}' = (\ddot{q}'_X, \ddot{r}'_Y, \ddot{\alpha}')^T.$$

The equations of motion for the two bodies can now be written as

$$M\ddot{r} = F^T \quad \text{and} \quad M'\ddot{r}' = F'^T, \tag{1}$$

where M and M' are, respectively, the mass matrices for H and H' given by

$$M = \begin{pmatrix} m & 0 & 0 \\ 0 & m & 0 \\ 0 & 0 & I \end{pmatrix} \quad \text{and} \quad M' = \begin{pmatrix} m' & 0 & 0 \\ 0 & m' & 0 \\ 0 & 0 & I' \end{pmatrix},$$

and F and F' are, respectively, the external forces and torques acting on H and H' given by

$$F = (F_X, F_Y, R) \quad \text{and} \quad F' = (F'_X, F'_Y, R').$$

Here m and m' are the masses and I and I' are the moments of inertia of H and H', respectively. Further F_X, F'_X and F_Y, F'_Y represent the force components in the $X-Y$ plane and R and R' are the external torques acting on H and H', respectively, as shown in Fig. 1(a).

2.1.2. Contact

Next we derive the equations of motion for the system when the two objects are in contact, as shown in Figs. 1(b) and (c). To do this we define a new coordinate system $n_1 - n_2$, rotated by an angle β about the origin relative to the coordinate system $X - Y$, where n_1 is the tangential vector to the contact plane and n_2 is the normal vector to the contact plane (see Fig. 1(d)). We also define $\theta = \alpha - \beta$ and $\theta' = \alpha' - \beta$ and let

$$q = (q_1, q_2, \theta)^T = (q_X \cos(\beta) - q_Y \sin(\beta), q_X \sin(\beta) + q_Y \cos(\beta), \alpha - \beta)^T,$$

and

$$q' = (q'_1, q'_2, \theta')^T = (q'_X \cos(\beta) - q'_Y \sin(\beta), q'_X \sin(\beta) + q'_Y \cos(\beta), \alpha' - \beta)^T.$$

Further, defining L as the distance from G to C and L' as the distance from G' to C, the positions q_C and q'_C of the contact point C relative to both bodies in the $n_1 - n_2$ frame can be written as

$$q_C := (q_1 - L\cos(\theta), q_2 - L\sin(\theta))^T \tag{2}$$

and

$$q'_C := (q'_1 - L'\cos(\theta'), q'_2 - L'\sin(\theta'))^T. \tag{3}$$

Note that we do not deal with the problem of finding the contact points in the general case but assume that there are well-defined contact points on each object. Let $d = q_C - q'_C$ be the relative distance between the contact points of the two bodies. Then the unilateral constraint between the two bodies is $d = (0,0)^T$ or equivalently when $q_C = q'_C$.

This is a useful framework to work with, particularly when deriving an impact mapping. It is also straightforward to translate back positions and angles to the original $X - Y$ coordinate system. The derivation of the impact mapping introduced in [28] splits contact forces into tangential and normal components in relation to the contact plane, i.e. using the $n_1 - n_2$ coordinate system. In order to relate how the contact forces will affect the centre of mass in terms of translations and rotations we need to consider

$$\frac{\partial q_C}{\partial q} = \begin{pmatrix} 1 & 0 & L\sin(\theta) \\ 0 & 1 & -L\cos(\theta) \end{pmatrix} \quad \text{and} \quad \frac{\partial q_C}{\partial q'} = \begin{pmatrix} 1 & 0 & L'\sin(\theta') \\ 0 & 1 & -L'\cos(\theta') \end{pmatrix}.$$

Now, the equations of motion for H and H' during contact can, respectively, be written as

$$M\ddot{q} = \hat{F}^T + \left(\frac{\partial q_C}{\partial q}\right)^T \lambda^T \tag{4}$$

and

$$M'\ddot{q}' = \hat{F}'^T + \left(\frac{\partial q_C}{\partial q'}\right)^T \lambda'^T, \tag{5}$$

where $\hat{F}$ and $\hat{F}'$ are, respectively, the external forces and torques acting on H and H' given by

$$\hat{F} = (F_1, F_2, R) = (F_X \cos(\beta) - F_Y \sin(\beta), F_X \sin(\beta) + F_Y \cos(\beta), R)\,,$$

and

$$\hat{F}' = (F_1', F_2', R') = (F_X' \cos(\beta) - F_Y' \sin(\beta), F_X' \sin(\beta) + F_Y' \cos(\beta), R')\,,$$

where the subscripts 1 and 2, respectively, represent the components of the external forces acting in the tangential and normal direction, and R and R' are as above the external torques acting on the bodies as shown in Fig. 1 (c). In a similar way we define λ and λ' as the forces generated at impact of each body given by

$$\lambda = (\lambda_1, \lambda_2) \quad \text{and} \quad \lambda' = (-\lambda_1, -\lambda_2)\,.$$

This setup is general and does not specify the mechanism that generates the tangential force λ_1. For this work however we assume that any tangential force arises due to friction at the contact point of the colliding bodies and here we use the Amontons-Coulomb friction law

$$\lambda_1 = \pm\mu\lambda_2 \tag{6}$$

for some non-negative constant μ representing a coefficient of friction. The sign assigned to the tangential force λ_1 is positive $(+)$ when the relative tangential contact point velocity between the two bodies is negative and it is negative $(-)$ when the relative tangential contact point velocity is positive.

2.2. Energetic Impact Law

For collisions between rigid bodies, dissipation of energy in the direction normal to the contact plane is modelled using a coefficient of restitution. A coefficient of restitution gives a relation between the normal impulse applied during the restitution phase to that applied during compression. Typically a Newtonian coefficient or a kinematic coefficient is used for this purpose [38], however, for situations where the direction of slip can vary throughout the impact phase both these coefficients will violate energy conservation [39]. Stronge [38] views the impact phase as being composed of a compression phase followed by a restitution phase. During compression, kinetic energy is stored as internal deformation energy until the normal relative contact point velocity is brought to zero. At this point the restitution phase begins and the stored energy is released.

For this purpose Stronge defines an energetic coefficient of restitution e_* as follows:

Definition 1. *The square of the coefficient of restitution is the negative ratio of the elastic strain energy released during restitution to the internal energy of deformation absorbed during compression,*

$$e_*^2 = -\frac{W(P_f) - W(P_c)}{W(P_c)},$$

where $W = \int_0^t F v \mathrm{d}t'$ and for a significantly short contact duration the force can be related to the differential of impulse, $\mathrm{d}P = F\mathrm{d}t'$ so that

$$e_*^2 = -\frac{\int_{P_c}^{P_f} v(P)\mathrm{d}P}{\int_0^{P_c} v(P)\mathrm{d}P}, \tag{7}$$

where P is the impulse, $v(P)$ is the relative normal velocity, $P_c = \int_0^{t_c} \lambda_N \mathrm{d}t$ is the normal impulse for compression, with t_c the time taken for the contact point velocity to reach zero, λ_N the normal component of the contact force and P_f is the final impulse achieved at separation.

This energetic restitution coefficient allows for the various stick-slip processes that can occur throughout the impact phase and thus is a restitution coefficient that will not violate energy conservation. It is notable that the kinematic and Newtonian coefficients do not allow for situations where the direction of slip can vary throughout the impact phase, and the consequence of this is that the final impulse is not calculated correctly. Further, the energetic restitution coefficient forms the basis for the impact mapping derived in [28], a brief description of which will be given below. When we refer to the impact phase we are considering velocity changes which occur as a function of normal impulse. This impulse formulation is a natural framework to use given that we assume the impact is of infinitesimal contact duration.

In order to map pre-impact velocities to post-impact ones it is necessary to consider the terminal impulse P_f for the given collision. Incorporating Amontons-Coulomb friction law (6) and the energetic restitution coefficient

(7) allows for a variety of stick-slip processes, each of which need to be considered and the corresponding P_f in each case determined. We will consider the equations of motion for a planar two-body collision. It is necessary to consider velocity changes as a function of normal impulse P instead of the time variable t. Consider (4) translated to the contact point q_C so that

$$\frac{d\dot{q}_C}{dt} = \frac{\partial q_C}{\partial q}\ddot{q} = \frac{\partial q_C}{\partial q}M^{-1}\left(\frac{\partial q_C}{\partial q}\right)^T \lambda^T + \frac{\partial q_C}{\partial q}M^{-1}F^T = w^{-1}\lambda^T + f(F_1, F_2, R, q, \dot{q}) \tag{8}$$

and

$$\frac{d\dot{q}_C}{dt} = \frac{\partial q_C}{\partial q'}\ddot{q} = \frac{\partial q_C}{\partial q'}(M')^{-1}\left(\frac{\partial q_C}{\partial q'}\right)^T \lambda'^T + \frac{\partial q_C}{\partial q'}(M')^{-1}F'^T = (w')^{-1}\lambda'^T + f'(F_1', F_2', R', q', \dot{q}'), \tag{9}$$

which is the rate of change of the contact point velocities as a function of time and where w^{-1} and $(w')^{-1}$ are the symmetric matrices given by

$$w^{-1} = \frac{\partial q_C}{\partial q}M^{-1}\left(\frac{\partial q_C}{\partial q}\right)^T = \begin{pmatrix} A & B \\ B & C \end{pmatrix},$$

$$(w')^{-1} = \frac{\partial q_C}{\partial q'}(M')^{-1}\left(\frac{\partial q_C}{\partial q'}\right)^T = \begin{pmatrix} A' & B' \\ B' & C' \end{pmatrix},$$

where

$$A = \frac{1}{m} + \frac{L^2\sin^2(\theta)}{I}, \quad B = \frac{-\sin(\theta)\cos(\theta)}{I}, \quad C = \frac{1}{m} + \frac{L^2\cos^2(\theta)}{I}$$

$$A' = \frac{1}{m'} + \frac{L'^2\sin^2(\theta')}{I'}, \quad B' = \frac{-\sin(\theta')\cos(\theta')}{I'}, \quad C' = \frac{1}{m'} + \frac{L'^2\cos^2(\theta')}{I'}.$$

In this context we do not need to consider terms which do not change throughout the impact phase and therefore we can neglect the functions f and f'. Further, during the impact phase we also have that

$$\frac{dP}{dt} = \lambda_2 \tag{10}$$

for H and by Newton's third law of motion

$$\frac{d(-P)}{dt} = -\lambda_2 \tag{11}$$

for H', since the normal impulse is a uniformly increasing scalar function during contact. Now, (8), (10) and (11) allow us to replace the independent variable t with P in (10) and (11) to give

$$\frac{d\dot{q}_C}{dP} = \frac{1}{\lambda_2}w^{-1}\begin{pmatrix} \lambda_1 \\ \lambda_2 \end{pmatrix}, \tag{12}$$

which is the rate of change of contact point velocities with respect to H as a function of normal impulse. In a similar way, using (9), (10) and (11), we also have

$$\frac{d\dot{q}_C'}{dP} = \frac{1}{\lambda_2}(w')^{-1}\begin{pmatrix} -\lambda_1 \\ -\lambda_2 \end{pmatrix}. \tag{13}$$

Subtracting (13) from (12) yields

$$\frac{d\dot{\tilde{q}}_C}{dP} := \frac{d\dot{q}_C}{dP} - \frac{d\dot{q}_C'}{dP} = \frac{1}{\lambda_2}\left(w^{-1} + (w')^{-1}\right)\begin{pmatrix} \lambda_1 \\ \lambda_2 \end{pmatrix}, \tag{14}$$

or in the notation of [28]

$$\frac{d\dot{\tilde{q}}_C}{dP} = \frac{1}{\lambda_2}\begin{pmatrix} \hat{A} & -\hat{B} \\ -\hat{B} & \hat{C} \end{pmatrix}\begin{pmatrix} \lambda_1 \\ \lambda_2 \end{pmatrix}, \tag{15}$$

which is the relative change in contact point velocities as a function of normal impulse. Expanding Eq. (15) and writing it in terms of tangential and normal components, respectively, gives

$$\frac{d\dot{\tilde{q}}_{1C}}{dP} = \hat{A}\frac{\lambda_1}{\lambda_2} - \hat{B}, \quad \frac{d\dot{\tilde{q}}_{2C}}{dP} = -\hat{B}\frac{\lambda_1}{\lambda_2} + \hat{C}, \tag{16}$$

which will be used to define the rate constants used for the impact mappings presented below.

Stronge [38] describes four possible impact-phase processes and calculates the terminal impulse and the post-impact velocity components for each phase. The four phases are:

Unidirectional slip during contact. In this case slip does not cease throughout the impact phase, and the tangential forcing acts in a direction opposite to the motion of the body.

Slip reversal during compression. In this situation initial sliding is brought to rest and then reverses direction.

Slip-stick transition during compression. The case whereby initial sliding is brought to rest. The contact point sticks if the friction coefficient μ is sufficiently large or undergoes reverse slip if it is not. It is also required that the initial sliding velocity is sufficiently small, otherwise this motion can not occur.

Jam. This is the process whereby there is an increase in normal acceleration at the contact point due to a large rotational acceleration. This motion occurs during an initial period of sliding.

Nordmark *et al.* [28] extend this theory by describing 10 different impact regions from which an impact law consisting of three mappings is derived. The impact mappings in [28] map the relative tangential and normal contact point velocities before the impact phase $\dot{\tilde{q}}_C^-$ to the post-impact phase velocities $\dot{\tilde{q}}_C^+$. Using Eq. (16) and following [28] we define the rate constants k_T^+, k_T^-, k_N^+, k_N^-, k_T^0 and k_N^0. These rate constants describe how stick and positive and negative slip can occur throughout the compression and restitution phase. For the various stick-slip processes described above Nordmark *et al.* [28] define the rate constants

$$k_T^+ = -\hat{B} - \mu\hat{A}, \quad k_N^+ = \hat{C} + \mu\hat{B},$$

$$k_T^- = -\hat{B} + \mu\hat{A}, \quad k_N^- = \hat{C} - \mu\hat{B},$$

$$k_T^0 = 0, \quad k_N^0 = \frac{\hat{A}\hat{C} - \hat{B}^2}{\hat{A}},$$

from which

$$k_T = \begin{cases} k_T^+, & \text{in positive slip,} \\ k_T^-, & \text{in negative slip,} \\ k_T^0, & \text{in stick,} \end{cases} \tag{17}$$

and

$$k_N = \begin{cases} k_N^+, & \text{in positive slip,} \\ k_N^-, & \text{in negative slip,} \\ k_N^0, & \text{in stick,} \end{cases} \tag{18}$$

can be determined, where $\mu = \frac{\lambda_1}{\lambda_2}$. It is worth mentioning that μ is taken as an absolute here and the rate constants described above consider all cases of positive and negative slip so it is not necessary to assign a sign to μ. Nordmark *et al.* [28] also define the constants k_T' and k_N', which are assigned one of the values of k_T^+, k_T^-, k_N^+, k_N^-, k_T^0 and k_N^0, and determined by the system parameters and pre-collision conditions. For full details we refer to [28]. From this and using Eq. (7) the following three maps, for pre-impact to post-impact contact point velocities $\dot{\tilde{q}}_C^- \mapsto \dot{\tilde{q}}_C^+$ can be derived:

Map I:

$$\dot{\tilde{q}}_{1C}^+ = \dot{\tilde{q}}_{1C}^- - (1 + e_*)\frac{k_T}{k_N}\dot{\tilde{q}}_{2C}^- \tag{19}$$

$$\dot{\tilde{q}}_{2C}^+ = -e_*\dot{\tilde{q}}_{2C}^- \tag{20}$$

Map II:

$$\dot{\tilde{q}}_{1C}^+ = \frac{k_T'}{k_N'}\left(\frac{k_N}{k_T}\dot{\tilde{q}}_{1C}^- - \dot{\tilde{q}}_{2C}^- + \sqrt{\left(1 - \frac{k_N'}{k_N}\right)\left(\frac{k_N}{k_T}\dot{\tilde{q}}_{1C}^- - \dot{\tilde{q}}_{2C}^-\right)^2 + {e_*}^2\frac{k_N'}{k_N}\left(\dot{\tilde{q}}_{2C}^-\right)^2}\right) \tag{21}$$

$$\dot{\tilde{q}}_{2C}^+ = \sqrt{\left(1 - \frac{k_N'}{k_N}\right)\left(\frac{k_N}{k_T}\dot{\tilde{q}}_{1C}^- - \dot{\tilde{q}}_{2C}^-\right)^2 + {e_*}^2\frac{k_N'}{k_N}\left(\dot{\tilde{q}}_{2C}^-\right)^2} \tag{22}$$

Map III:

$$\dot{\tilde{q}}_{1C}^{+} = \frac{k'_T}{k'_N}\left(\frac{k_N}{k_T}\dot{\tilde{q}}_{1C}^{-} - \dot{\tilde{q}}_{2C}^{-} + e_*\sqrt{\left(1-\frac{k'_N}{k_N}\right)\left(\frac{k_N}{k_T}\dot{\tilde{q}}_{1C}^{-} - \dot{\tilde{q}}_{2C}^{-}\right)^2 + {e_*}^2\frac{k'_N}{k_N}\left(\dot{\tilde{q}}_{2C}^{-}\right)^2}\right) \quad (23)$$

$$\dot{\tilde{q}}_{2C}^{+} = e_*\sqrt{\left(1-\frac{k'_N}{k_N}\right)\left(\frac{k_N}{k_T}\dot{\tilde{q}}_{1C}^{-} - \dot{\tilde{q}}_{2C}^{-}\right)^2 + \frac{k'_N}{k_N}\left(\dot{\tilde{q}}_{2C}^{-}\right)^2} \quad (24)$$

for $k_N \neq 0$ and

$$\dot{\tilde{q}}_{1C}^{+} = 0 \quad (25)$$

$$\dot{\tilde{q}}_{2C}^{+} = e_*\sqrt{\left(\dot{\tilde{q}}_{2C}^{-}\right)^2 + \frac{2k'_N\dot{\tilde{q}}_{1C}^{-}\dot{\tilde{q}}_{2C}^{-}}{k_T}} \quad (26)$$

for $k_N = 0$.

As mentioned above, the different combinations of segments of stick and relative slip can be described by ten different regions, each of which corresponds to one of the three maps given above. It is worth noting that in [40] an equivalent energetic coefficient of restitution is used together with the Amontons-Couloumb friction law to describe the contact and impact dynamics for the case of a bouncing dimer.

2.3. Dynamics

As the type of mechanical system considered for this work is unconstrained away from the discontinuity surfaces, various possible modes of sustained motion can occur. To highlight this, in Fig. 2 we consider a schematic of the time history of a point $p(t)$ on a rigid body that occasionally acts as a contact point during impacts with a non-compliant surface. We only need to define three modes of motion, namely, unconstrained free flight, chatter and

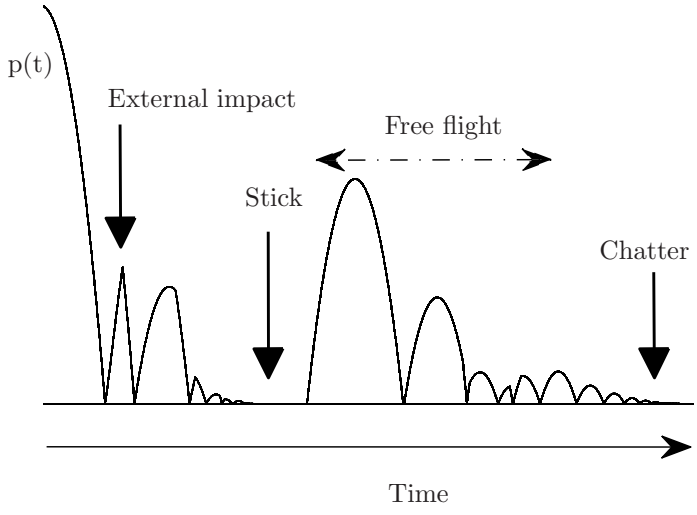

Figure 2: A schematic detailing the time history of a contact point $p(t)$ in an impacting system.

stick. For our purposes, unconstrained free flight could describe, for example, the motion of a projectile that is free to rotate about all axes and is entirely unconstrained. Note that constrained free flight could describe, for example, the motion of a double pendulum. The system is constrained to move in a plane with two degrees of freedom due to the upper arm of the pendulum being constrained to a fixed point. It is also necessary to distinguish between two types of chatter, namely, complete and incomplete chatter [31]. Complete chatter is where an object undergoes an infinite number of impacts in finite time and eventually transitions to stick. This motion can be observed in

reality where a bouncing a ball, for example, undergoes a large number of impacts and eventually comes to a stop and transitions into a stick state. Incomplete chatter is where the system undergoes a large number of impacts in a short time frame but transitions to free flight due to a change in the relative acceleration.

At an impact, after free flight, a system can evolve in a number of different ways: It can continue in free flight motion, go into a stick regime or go through a chatter sequence. A feature which is also present in the schematic Fig. 2 is an *External impact*, where another point of the rigid-body system impacts and thus causes a change in the dynamics of the point $p(t)$. For analysis purposes it is important to be able to distinguish between the different features and subtle changes in order to understand the mechanisms that cause them. There are typically also a number of system-specific long-term dynamical behaviours present. In Section 4.1 and 4.3 we discuss such examples for the case of a slender rod impacting an oscillating surface.

3. Numerical methods

In this section we will give a very brief description of the different numerical methods employed for simulation of the rigid-body system with impacts and friction described in Section 4. We mainly follow the methodologies described in [31] and [36] with some extensions and some simplifications, as we will describe below. The methodology we use here is, as mentioned in Section 1, sometimes referred to as the hybrid or event-driven approach, where continuous dynamics, described by a system of smooth ODEs, is combined with discrete events, described by maps. The maps are used when a solution trajectory reaches an *event surface* defined by the system variables and parameters. In this context we consider the continuous dynamics as the motion between the impacts or other transitions and the maps correspond to the actual impacts or transitions. The transitions are typically changes from free-flight dynamics to stick or to chatter.

To solve a system of smooth ODEs in Section 4 we mainly use the MATLAB's ODE solver `ode45` and to locate the event surfaces we use MATLAB's built-in event-detection routines. However, the methodology described here can equally well be implemented in any environment that has an ODE solver and event location capabilities. The ODE solver requires at least two vector fields (one for the free-flight phase and one for stick, but see further Section 4 for a specific implementation), simulation times, initial conditions, error tolerances and integration step sizes. In order to accurately locate the event surfaces, event functions need to be described that are derived from the geometries of the impacting rigid bodies. Finally, impact maps, like those described in Section 2.2 have to be defined together with a process that determines what impact map to use for the specific impact.

In general, when dealing with rigid bodies, it is more than likely that the overall system can have multiple contact points and a large number of events can occur (impacts or vector field transitions). These two factors can generally give rise to a number of computational complications, making the analysis of long-term dynamics difficult. One such useful example is to define an additional artificial term on the vector fields that makes the surface locally attractive when the system is in stick. This ensures that the contact point does not drift away from the surface due to numerical errors. A similar approach was used in [36] for Filippov systems.

Following the setup of system states presented in [36, 31] we can achieve a robust numerical code capable of simulating the system to examine long-term dynamics. By robust we mean, using this method, the numerical simulator is capable of handling the events and transitions which can occur, without breaking down. This is presented in Section 3.1, followed by a discussion in Section 3.2 on brute-force bifurcation analysis in general and stability analysis of symmetric period-1 solutions.

3.1. System States

One of the many difficulties associated with using a hybrid strategy for finding the solution to a dynamical system with discontinuities is the accumulation of events, for instance when an incomplete or a complete chattering sequence is encountered (see Section 2.3 and [4]). To deal with this in a systematic manner it is advantageous to introduce the notion of system states in a similar way as was done in [36, 31]. For a general system we can define n discrete states S_n in which one of the defined vector fields Φ_n is being used. Each vector field Φ_n either corresponds to free-flight or sticking motion, which has to be defined by the user. A transition diagram can be used to decide if a system should transition from one state to another at an event, and also provides a means for numerically dealing with a complete chatter sequence.

The number of free-flight and stick states depends mainly on the geometry of the impacting rigid bodies. This point will be illustrated further in Section 4.2 for a model example showing a slender rod impacting an oscillating plane.

The mechanism for switching between the states S_n at impact involves evaluating relative normal contact point accelerations and velocities, whereafter a transition diagram together with a decision tree can be used to evaluate

what state the system should be in after the impact. The contact point velocities are mainly used to calculate post-impact velocities. This is in contrast to the contact point accelerations that are used to determine when the system should release from stick to free flight. The specific implementations have to be assessed on a case-by-case basis.

3.2. Bifurcation diagrams and stability analysis

A common way in which to make an initial assessment of the long-term dynamics of a mechanical system is to plot brute-force bifurcation diagrams. In Section 4.3 we highlight some aspects of how the long-term dynamics of a mechanical system with impacts is affected by friction through bifurcation diagrams. The bifurcation diagrams shown in Section 4.3 are made up of, on the one hand, period-1 solutions found by a semi-analytic continuation method based on a shooting method and, on the other hand, other recurrent motions found by brute-force simulation methods. For the period-1 solutions the stabilities are found by calculating the eigenvalues of the fundamental solution matrix that is found by solving the variational equations of the piecewise-smooth system. For this purpose saltation matrices are used to merge together fundamental solution matrices for trajectories that switch from one state to another. These methods have successfully been implemented in [2, 13, 34] and particularly in [31] which reports the stability analysis for impacting systems without friction but with complete chatter.

4. Dynamics of a slender rod impacting a periodically-oscillating surface

In this section we will use a basic planar model of a rigid slender rod impacting a periodically oscillating surface to illustrate the techniques discussed in Section 2. The model will also be used to describe how the numerical methods discussed in Section 3 can be implemented and what the dynamical features presented in Section 2.3 look like for this specific case. We will also use this setup to show how friction affects chaotic rattling behaviour of the rod.

4.1. The model, system states and vector fields

As discussed above we consider a planar uniform slender rigid rod and let q_1, q_2 be the tangential and normal position of the centre of mass, relative to the contact plane, and let θ be the angle of rotation of the rod (see Fig. 3(a)). For this model example the tangential and normal direction correspond to the n_1 and n_2 directions, respectively, as discussed in Section 2 and shown in Fig. 1. The rod is subjected to gravity and where either of the two isolated end points, named P_1 and P_2, can impact, get stuck to or slide along the periodically oscillating surface. The slender rod can essentially be in four different states: free flight (Fig. 3(a)), one of the two end points is stuck to the surface (Fig. 3(b) and (c)), or both end points are stuck to the surface (Fig. 3(d)). The fourth state here also allows for the release of the two end points at the same time, which in effect leads to a lower-dimensional dynamical system that can be treated as a simple impacting particle.

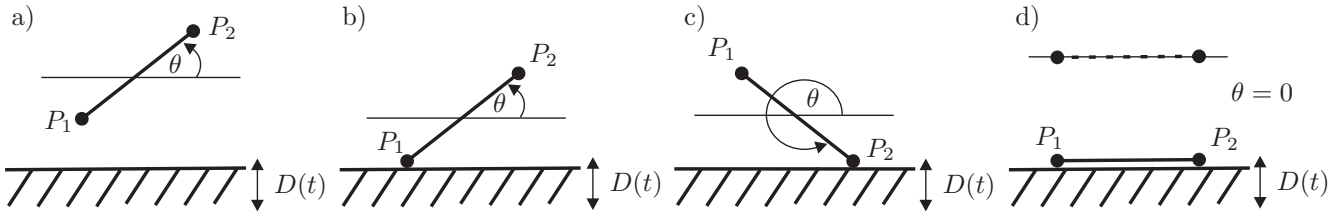

Figure 3: The four possible main states of the slender rod. (a) Free-flight motion. (b) End point P_1 constrained to the surface. (c) End point P_2 constrained to the surface. (d) Symmetric free-flight motion (dashed) and symmetric stick motion (solid).

Without loss of generality and following the general setup in Section 2, we let the mass of the rod be $m = 1$ and the distance from the centre of mass to either of the two end points be $L = 1$. This gives the moment of inertia $I = \frac{1}{3}$ and the radius of gyration $k_r^2 = \frac{1}{3}$. We further assume that the vertically oscillating surface is not affected by the rod at impact and thus let $D(t)$ represent the oscillating surface with frequency ω, amplitude A and where t is time, so that $D(t) := A\sin(\omega t)$ (see Fig. 3). This means that we only need to consider one of the two impacting bodies introduced in Section 2.1.1 as the mass of the surface can be assumed to be much greater than that of the rod and thus only one of the two systems of differential equations, say Eq. (4), needs to be considered. For future reference we let $q_4 = \dot{q}_1, q_5 = \dot{q}_2, q_6 = \dot{\theta}$ and introduce τ as the phase of the oscillating floor. We also let d_1 be the distance between the end point P_1 and the surface in the normal direction and let d_2 be the distance between the

end point P_2 and the surface in the normal direction. The unilateral constraints for this model example are thus $d_1 = 0$ (see Fig. 3 (b)),or $d_2 = 0$ (see Fig. 3 (c)) or simultaneously $d_1, d_2 = 0$ (see Fig. 3 (d)). Further, using Eq. (2) we find

$$d_1 = q_2 - \sin(\theta) - A\sin(\omega t), \tag{27}$$
$$d_2 = q_2 + \sin(\theta) - A\sin(\omega t),$$

from which we obtain the relative velocity between the end point P_1 and the floor as

$$\dot{d}_1 = \dot{q}_2 - \cos(\theta)\dot{\theta} - A\omega\cos(\omega t), \tag{28}$$

and the relative velocity between the end point P_2 and the floor as

$$\dot{d}_2 = \dot{q}_2 + \cos(\theta)\dot{\theta} - A\omega\cos(\omega t),$$

the relative acceleration between the end point P_1 and the floor as

$$\ddot{d}_1 = \ddot{q}_2 + \sin(\theta)\dot{\theta}^2 - \cos(\theta)\ddot{\theta} + A\omega^2\sin(\omega t), \tag{29}$$

and the relative acceleration between the end point P_2 and the floor as

$$\ddot{d}_2 = \ddot{q}_2 - \sin(\theta)\dot{\theta}^2 + \cos(\theta)\ddot{\theta} + A\omega^2\sin(\omega t).$$

Now, we are ready to introduce the five system states, which we will use for simulating this mathematical model of the planar rod, together with the corresponding vector fields.

State 1 – Free flight. Since we make the assumption that there is no external torque or no horizontally acting forcing present, we have that $R = 0$ and $F_1 = 0$ in Eq. (4). The only external force acting in the vertical direction is due to gravity, and so $F_2 = -g$. Following this, the equations of motion of the rod in free flight is given by

$$\ddot{q}_1 = 0, \tag{30}$$
$$\ddot{q}_2 = -g, \tag{31}$$
$$\ddot{\theta} = 0, \tag{32}$$

and the corresponding dynamical system is

$$(\dot{q}_1, \dot{q}_2, \dot{\theta}, \dot{q}_4, \dot{q}_5, \dot{q}_6, \dot{\tau})^T = (q_4, q_5, q_6, 0, -g, 0, 1)^T := \Phi_1(t)$$

that will be used for the numerical simulation of the free-flight motion. Notice that we have included the phase τ in the dynamical system in order to have better control of the periodic influence of time.

State 2 – End point P_1 is stuck to the floor. We will derive a new vector field for the system when P_1 is stuck to the floor. First, from Eq. (4) we get that the equations of motion for the constrained bar is

$$\ddot{q}_1 = \lambda_1, \tag{33}$$
$$\ddot{q}_2 = -g + \lambda_2, \tag{34}$$
$$\ddot{\theta} = 3\sin(\theta)\lambda_1 - 3\cos(\theta)\lambda_2. \tag{35}$$

Next, we need to find the forces λ_1 and λ_2 needed to constrain P_1 to the oscillating surface. Substituting Eq. (34) and Eq. (35) into Eq. (29) and using the Amontons-Coulomb friction law $\lambda_1 = s\mu\lambda_2$ gives

$$\ddot{d}_1 = -g + \lambda_2 + \sin(\theta)\dot{\theta}^2 - 3\cos\theta\sin(\theta)s\mu\lambda_2 + 3\cos^2(\theta)\lambda_2 + A\omega^2\sin(\omega t), \tag{36}$$

where s is either $+1$ or -1, depending on the relative tangential velocity at impact. Further, using the fact that $d_1 = \dot{d}_1 = \ddot{d}_1 = 0$ when the end point P_1 is in contact with the surface and solving for λ_2 gives

$$\lambda_2 = \frac{g - \sin(\theta)\dot{\theta}^2 - A\omega^2\sin(\omega t)}{1 + 3\cos^2(\theta) - 3s\cos(\theta)\sin(\theta)\mu}, \tag{37}$$

which is the normal forcing required to ensure that the contact point will remain constrained to the plane.

Last, we can write the vector field for the rod with the end point P_1 stuck to the floor as

$$(\dot{q}_1, \dot{q}_2, \dot{\theta}, \dot{q}_4, \dot{q}_5, \dot{q}_6, \dot{\tau})^T = (q_4, q_5, q_6, \alpha_1, \alpha_2, \alpha_3, 1)^T := \Phi_2(t)$$

where

$$\begin{aligned}
\alpha_1 &= \frac{s\mu\left(g - \sin(\theta)\dot{\theta}^2 - A\omega^2\sin(\omega t)\right)}{1 + 3\cos^2(\theta) - 3s\mu\cos(\theta)\sin(\theta)},\\
\alpha_2 &= -g + \frac{g - \sin(\theta)\dot{\theta}^2 - A\omega^2\sin(\omega t)}{1 + 3\cos^2(\theta) - 3s\mu\cos(\theta)\sin(\theta)},\\
\alpha_3 &= \frac{(3s\mu\sin(\theta) - 3\cos(\theta))\left(g - \sin(\theta)\dot{\theta}^2 - A\omega^2\sin\omega t\right)}{1 + 3\cos^2(\theta) - 3s\mu\cos(\theta)\sin(\theta)}.
\end{aligned}$$

State 3 – End point P_2 is stuck to the floor. Similarly, using symmetry, we can write the vector field for the rod with the end point P_2 stuck to the floor as

$$(\dot{q}_1, \dot{q}_2, \dot{\theta}, \dot{q}_4, \dot{q}_5, \dot{q}_6, \dot{\tau})^T = (q_4, q_5, q_6, \alpha_4, \alpha_5, \alpha_6, 1)^T := \Phi_3(t)$$

where

$$\begin{aligned}
\alpha_4 &= \frac{s\mu\left(-g + \sin(\theta)\dot{\theta}^2 - A\omega^2\sin(\omega t)\right)}{3s\mu\cos\theta\sin(\theta) - 1 - 3\cos^2(\theta)},\\
\alpha_5 &= -g + \frac{-g + \sin(\theta)\dot{\theta}^2 - A\omega^2\sin(\omega t)}{3s\mu\cos\theta\sin(\theta) - 1 - 3\cos^2(\theta)},\\
\alpha_6 &= \frac{(3s\mu\sin(\theta) - 3\cos(\theta))\left(-g + \sin(\theta)\dot{\theta}^2 - A\omega^2\sin(\omega t)\right)}{3s\mu\cos\theta\sin(\theta) - 1 - 3\cos^2(\theta)}.
\end{aligned}$$

State 4 – Symmetric motion. We define symmetric motion as one where $\theta \mod \pi = q_6 = 0$ for all time, which means that the two end points will impact the floor at the same time. The dynamical system will be the same as in the free-flight case albeit the motion is heavily constrained, and thus the vector field Φ_1 can be used.

State 5 – Both end points P_1 and P_2 stuck to the floor. If both end points are stuck to the floor it means that the centre of mass will oscillate as $D(\tau)$ and thus the vector field in this case is trivially

$$(\dot{q}_1, \dot{q}_2, \dot{\theta}, \dot{q}_4, \dot{q}_5, \dot{q}_6, \dot{\tau})^T = (q_4, q_5, q_6, 0, -\omega^2 A\sin(\omega\tau), 0, 1)^T := \Phi_4.$$

4.2. State transitions and impact mappings

For the planar rod model described above in Section 4.1 we introduced five system states, two for free flight and three for stick. Our proposed scheme for dealing with chatter involves constraining the respective end point to the impact surface when that corresponding end point is going through a chatter sequence. The system then acts as a sliding hinge. For this purpose we define the critical normal contact point relative velocity as V_{tol} and use this, along with the end point accelerations, as criteria for deciding when the system is going through a chatter sequence. V_{tol} is chosen based on the system in question and what makes physical sense. In this paper we typically let V_{tol} be $\leq 10^{-6}$. When an impact occurs the critical normal contact point relative velocities $\dot{d}_1$ and $\dot{d}_2$ together with the critical normal contact point relative accelerations $\ddot{d}_1$ and $\ddot{d}_2$ are evaluated. These values are then used with a decision tree to decide if the system should transition to another state. It is important to note that when calculating the relative contact point accelerations when in a stick state, we use the unconstrained values. This approach ensures that the system will naturally release from stick due to the change in relative acceleration. At impact the impact law needs to be applied to determine what type of transition should occur. For the model example described here the rate constants defined in Section 2.2 now take the form

$$k_T^+ = -3\sin(\theta)\cos(\theta) - \mu\left(1 + 3\sin^2(\theta)\right), \quad k_N^+ = 1 + 3\cos^2(\theta) + 3\mu\sin(\theta)\cos(\theta)$$

for positive slip,

$$k_T^- = -3\sin(\theta)\cos(\theta) + \mu\left(1 + 3\sin^2(\theta)\right), \quad k_N^- = 1 + 3\cos^2(\theta) - 3\mu\sin(\theta)\cos(\theta)$$

for negative slip, and

$$k_{T0} = 0, \quad k_{N0} = \frac{4}{1 + 3\sin^2(\theta)}$$

for the stick regime. These rate constants are used in the mappings for the numerical implementation together with a decision tree. The process involves deciding what region the impact corresponds to depending on initial conditions and assigning the corresponding rate constants and impact map accordingly, see further [28]. However, apart from deciding what will happen at a specific impact the system can also switch between the different states described in Section 4.1. The transition diagram describing what transitions are possible for the rod system are given in Fig. 4, where $S_1 - S_5$ are the states introduced in Section 4.1.

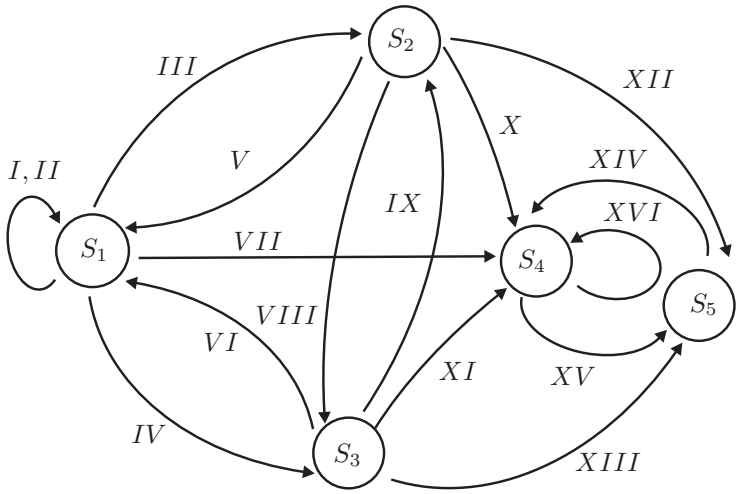

Figure 4: A transitions diagram for the planar rod system showing the five states, $S_1 - S_5$ and the state transitions $I - XVI$. See also Table 1 for a list of event types and transition criteria.

Transition	Type	Event	Transition Criteria	Contact angle θ	State
I	I	$d_1 = 0$	$\lvert\dot{d}_1\rvert > V_{tol}$,	$\neq 0$	$S_1 \to S_1$
II	I	$d_2 = 0$	$\lvert\dot{d}_2\rvert > V_{tol}$	$\neq 0$	$S_1 \to S_1$
III	C	$d_1 = 0$	$\lvert\dot{d}_1\rvert < V_{tol}$,	$\neq 0$	$S_1 \to S_2$
IV	C	$d_2 = 0$	$\lvert\dot{d}_2\rvert < V_{tol}$	$\neq 0$	$S_1 \to S_3$
V	R	$\ddot{d}_1 > 0$		$\neq 0$	$S_2 \to S_1$
VI	R	$\ddot{d}_2 > 0$		$\neq 0$	$S_3 \to S_1$
VII	L	$d_1 = 0$, $d_2 = 0$	$\lvert\dot{d}_{1,2}\rvert > V_{tol}$, $\theta \mod \pi < \theta_{Crit}$	0	$S_1 \to S_4$
VIII	TR	$\ddot{d}_2 > 0$		0	$S_2 \to S_3$
IX	TR	$\ddot{d}_1 < 0$		0	$S_3 \to S_2$
X	T	$d_2 = 0$	$\lvert\dot{d}_2\rvert > V_{tol}$	0	$S_2 \to S_4$
XI	T	$d_1 = 0$	$\lvert\dot{d}_1\rvert > V_{tol}$	0	$S_3 \to S_4$
XII	TC	$d_2 = 0$	$\lvert\dot{d}_2\rvert < V_{tol}$	0	$S_2 \to S_5$
XIII	TC	$d_1 = 0$	$\lvert\dot{d}_1\rvert < V_{tol}$	0	$S_3 \to S_5$
XIV	R	$\ddot{d}_{1,2} > g$		0	$S_5 \to S_4$
XV	TC	$d_1 = 0$, $d_2 = 0$	$\lvert\dot{d}_1\rvert < V_{tol}$, $\lvert\dot{d}_2\rvert < V_{tol}$	0	$S_4 \to S_5$
XVI	T	$d_1 = 0$, $d_2 = 0$	$\lvert\dot{d}_1\rvert > V_{tol}$, $\lvert\dot{d}_2\rvert > V_{tol}$	0	$S_4 \to S_4$

Table 1: Table corresponding to the transition diagram in Fig. 4. The different types of transitions are I - Impact, C - Chatter, R - Release, L - Limit,T - Two-point impact, TR - Two-point impact with Release and TC - Two-point impact with Chatter.

A summary of all states and transitions are given in Table 1 and brief descriptions of the 16 transitions (I - XVI) in Fig. 4 are given here:

Transition I. Impact of end point P_1 with $|\dot{d}_1| > V_{tol}$. The system will remain in free flight State 1.

Transition II. Impact of end point P_2 with $|\dot{d}_2| > V_{tol}$. The system will remain in free flight State 1.

Transition III. If at impact $|\dot{d}_1| < V_{tol}$. The system will transition to stick State 2.

Transition IV. If at impact $|\dot{d}_2| < V_{tol}$. The system will transition to stick State 3.

Transition V. If at any moment during the constrained motion $\ddot{d}_1 > 0$, then the system will transition to free flight State 1.

Transition VI. If at any moment during the constrained motion $\ddot{d}_2 > 0$ then the system will transition to free flight State 1.

Transition VII. In the limiting case where the impact angle θ approaches zero with each impact and eventually reaches a predefined threshold in which the angle can be assumed to be zero. The system transitions to the symmetric State 4.

Transition VIII. If at impact $\ddot{d}_1 > 0$ and $\ddot{d}_2 < 0$, then the system will transition to stick State 3.

Transition IX. If at impact $\ddot{d}_2 > 0$ and $\ddot{d}_1 < 0$, then the system will transition to stick State 2.

Transition X. If at impact $|\dot{d}_2| > V_{tol}$, then the system transitions to the symmetric State 4.

Transition XI. If at impact $|\dot{d}_1| > V_{tol}$, then the system transitions to the symmetric State 4.

Transition XII. If at impact $|\dot{d}_2| < V_{tol}$, then the system will transition to the symmetric stick State 5.

Transition XIII. If at impact $|\dot{d}_1| < V_{tol}$, then the system will transition to the symmetric stick State 5.

Transition XIV. The system will remain in State 5 unless the frequency of oscillation exceeds a critical value ω^* given by $\omega^* = \sqrt{\frac{g}{A\sin(\omega\tau)}}$. When this value is exceeded the system will release from stick and transition to the symmetric State 4. For a given ω value, ω^* will vary sinusoidally depending on the phase of oscillation τ. When the floor acceleration is maximal, ω^* will be minimized, and when the floor acceleration is minimal, ω^* will be maximized.

Transition XV. If $\ddot{d}_{1,2} < 0$ or $|\dot{d}_{1,2}| < V_{tol}$, then the system will transition to the symmetric stick State 5.

Transition XVI. If at impact $\ddot{d}_{1,2} > 0$, $\dot{d}_1 > V_{tol}$ and $\dot{d}_2 > V_{tol}$ the system will remain in State 4.

4.3. Results

Here we will focus on the numerical analysis of some aspects of the long-term dynamics of the impacting rod introduced in Section 4.1. The purpose of this is twofold. First, we want to show the robustness of the numerical techniques presented in Sections 4.1 and 4.2, and second, we want to display some of the behaviour that one can expect from a rattling object where energy that is dissipated both through the impact and friction. In this context we will focus both on steady-state dynamics and transients.

As discussed in Section 4.1 and shown in Fig. 3 the system can essentially be in five different states between events (impacts or transitions). On top of this numerical experiments have shown that the more energy that is removed from the system at impact through friction the faster the system tends from asymmetric to symmetric motion (see Fig. 5). In terms of the model example presented in this work, asymmetric chaos refers to chaotic motion when in State 1, and symmetric chaos refers to chaos when in State 4. This indicates that if the energy that is added into the system is acting in the normal direction relative to the impact then the friction, which only acts in the tangential direction, will reduce the rotational energy over time and only symmetric motion will remain. To highlight this the example in Fig. 5(a) shows a time history of the angle θ when the system goes through a transition from asymmetric to symmetric motion. Recall that $\theta = 0$ or $\theta = \pi$ means that the rod is aligned parallel to the surface. In Fig. 5(b) we see a close up of how the actual transition in this case happens over a very short time interval. In principal it is an accumulation of alternative impacts between the two ends, i.e. very similar to what we see in complete chatter, but here we do not necessarily have stick. In Fig. 5(c) we see a similar example, where the time history of the position of each of the two end points are shown to highlight how the transition between transient asymmetric chaos and transient symmetric chaos can occur. We note that up to approximately $t = 302$ there are two separate trajectories, one for each end point, but suddenly the two trajectories converge and the two end points move in synchrony and the rotation of the rod ends. The figure also indicates that the system stays chaotic but where all the rotational energy has dissipated due to friction. This will not always be the case however, as seen in Figs. 6 (a) and (b). After $t = 790$ the system still remains in asymmetric chaos. A comparison of Fig. 6 (b) with Fig. 5(c) shows the difference between asymmetric and symmetric chaos. In Fig. 6 (b) the system

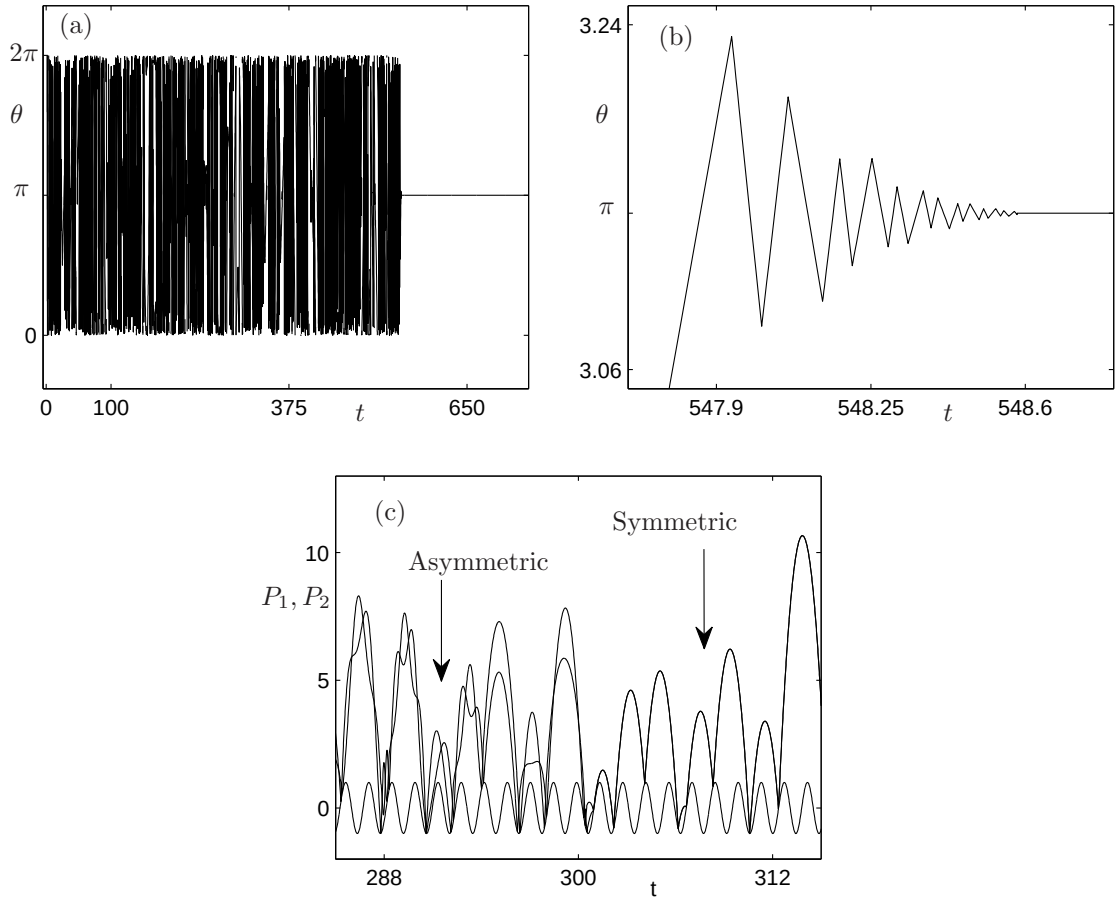

Figure 5: Time histories showing (a) the rod angle $\theta \mod 2\pi$, (b) a close-up of (a) showing the transition from asymmetric to symmetric motion, and (c) the surface $S(t)$ and the end points $P_1(t)$ and $P_2(t)$ for the rod before and after the transition from asymmetric to symmetric motion occurs. Here $\omega = 4.4050$, $e_* = 0.8$, $A = 1$ and $\mu = 0.05$.

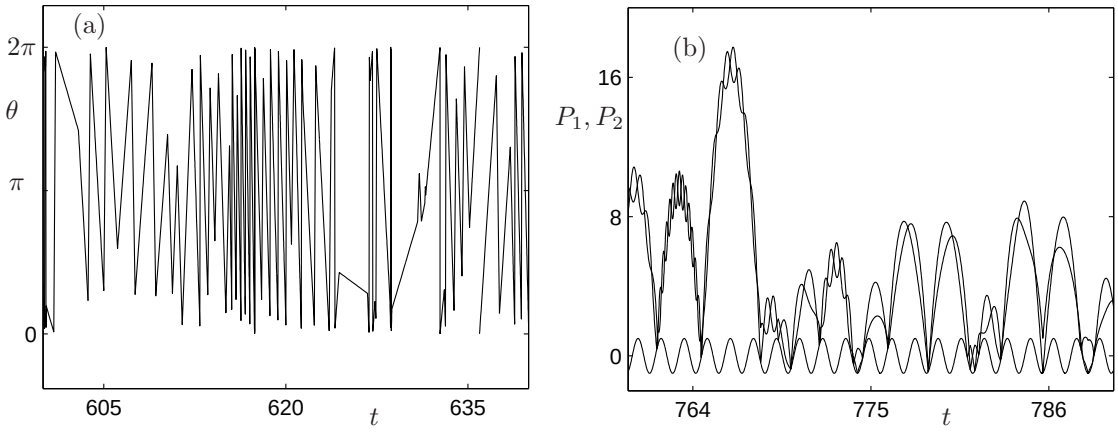

Figure 6: Time histories showing (a) the rod angle $\theta \mod 2\pi$ and (b) the contact points $P_1(t)$ and $P_2(t)$ for $\omega = 4.40572$, $e_* = 0.9$, $A = 1$ and $\mu = 0.5$.

has still not reached symmetric chaos (transitioned to state 4) and it is possible that it never will. In Fig. 5(c) the system has reached symmetric chaos (transitioned to state 4).

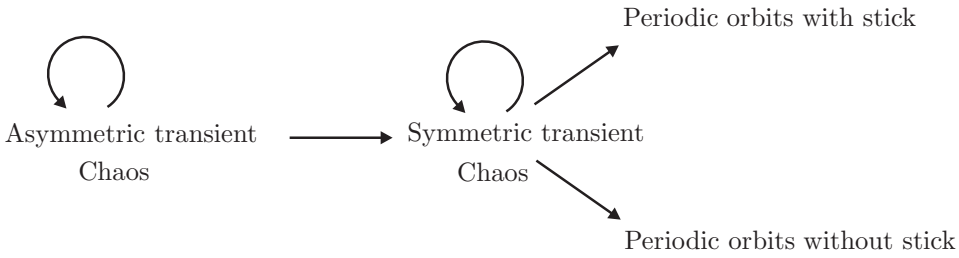

Figure 7: A schematic detailing the possible transitions from transient asymmetric chaos to transient symmetric chaos and periodic orbits that can occur in the system.

In Fig. 7 a schematic transition diagram for transient motions found in the rod system is shown. Note that this schematic is based on observations from numerical experiments of the rod system and not on analytically derived conditions. In many cases, for general initial conditions, the rod system undergoes motion akin to asymmetric chaos until the rotational energy has dissipated and the symmetric (transient) chaos takes over. Depending on the frequency of the external forcing the symmetric chaos may persist or the motion turn periodic. Again, depending on the frequency and the value of the restitution coefficient the periodic orbits may have periods of stick. The effect of this is that, at least for low frequencies ω, all long term motions that we have come across, are symmetric and thus brute-force bifurcation diagrams only show stable solutions, where the dynamics is symmetric. It is worth noting that in the limit, where the impact times between the end points as well as the tangential impact velocities go to zero, Map I (see Section 2.2) is succesively applied and once the transition to symmetric motion has occured Map I reduces to the standard Newtonian restitution law, which is in-line with what is discussed in [28]. For the rod system in question this means that the long term behavior can simply be approximated by a one-dimensional system of a mass impacting an oscillating surface. While the general one-dimensional system has been analysed before, see particularly Holmes [20], we will present some specific results for the system analysed here in order to give us an idea on what we can predict regarding the long-term behaviour for specific parameter values.

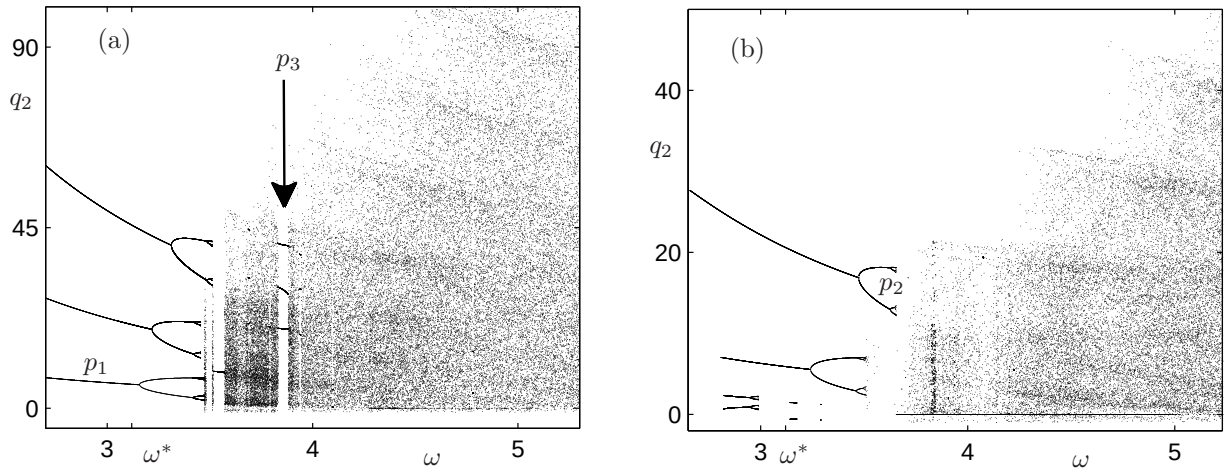

Figure 8: Bifurcation diagrams showing how the steady-state of the position of the centre of mass q_2 varies as the frequency ω is varied. In (a) $e_* = 0.9$, $A = 1$ and $\mu = 0.05$ and in (b) $e_* = 0.8$, $A = 1$ and $\mu = 0.05$. The period-1 orbit is labeled in (a) and the period-2 and period-3 orbits are labeled in (b).

To describe how possible transitions between different types of long-term motion in the symmetric (one-dimensional) rod system occur we show in Fig. 8 (a) and (b) two brute-force bifurcation diagrams, ω vs. q_2, for two different values of the restitution coefficient, $e_* = 0.9$ and $e_* = 0.8$, respectively. Fig. 8(a) shows three coexisting period-1 solutions that undergo period-doubling sequences, at three different values of ω, until the branches disappear in grazing bifurcations at $\omega \approx 3.5$. The figures also shows that regions of chaos start at $\omega \approx 3.5$, with two periodic windows (a period-1 and a period-3 orbit, see Fig. 9(a)) also existing within the chaos. The bifurcation

diagram in Fig. 8(b), where the restitution coefficient is lower, we see that the onset of chaos occurs at $\omega \approx 3.8$ and thus the periodic orbits are sustained longer when more energy is taken out of the systems at impact. To show what some of the symmetric period-1 solutions look like in Fig. 9(a) a time series of the end points of the period-1 orbit highlighted as p_1 in Fig. 8(a) (p_1) is shown. In Fig. 9(b) a time series of the end points of the period-2 orbit highlighted as p_2 in Fig. 8(b) is shown. Similarly in Fig. 9(c) a time series of the end points of the period-3 orbit highlighted as p_3 in Fig. 8(a) is shown. This shows that freely rattling objects subject to periodic forcing have co-existing recurrent motions, periodic and/or chaotic, as has been shown before [20]. The three co-existing period-1 orbits in Fig. 8(a) are reached from different initial conditions, i.e. the rod system is initially impacting the surface at different phases of the surface oecillation. The time history illustrated in Fig. 9 (c) corresponds to initial conditions taken from the the period-1 orbit in Fig. 8.

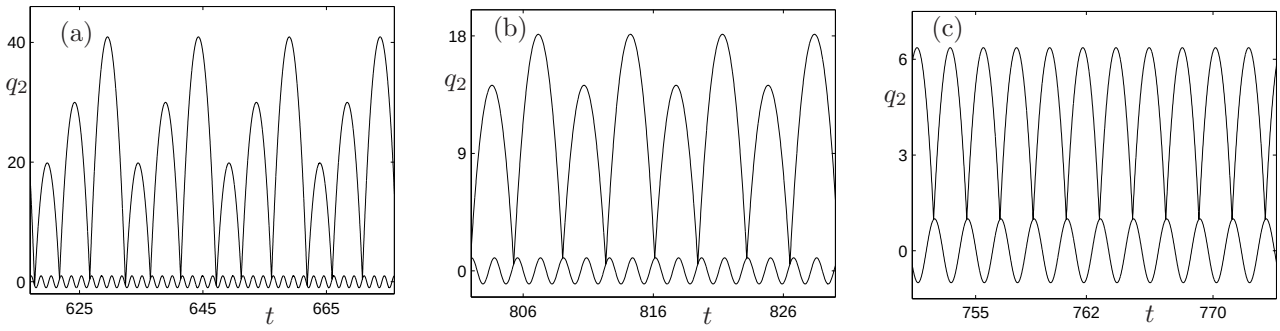

Figure 9: Time histories for q_2 showing (a) a period-3 solution (see label p_3 in Fig. 8(a)), (b) a period-2 solution (see label p_2 in Fig. 8(b)) and (c) a period-1 solution (see label p_1 in Fig. 8(a)). In (a) and (c) $\omega = 3.0$, $e_* = 0.9$, $A = 1$ and $\mu = 0.05$ and in (b) $\omega = 3.55085$, $e_* = 0.8$, $A = 1$ and $\mu = 0.05$.

A useful technique for understanding the long-term behaviour in this system is to examine how the period-1 solutions behave under parameter variations. In Fig. 10(a) we plot bifurcation diagrams using continuation methods for five different e_* values under ω variation. The figure shows that period-1 orbits are born at a smaller frequency ω the bigger the e_* value is. It seems obvious that if less energy is taken out at impact then less energy is needed from the oscillating surface to sustain a similar periodic orbit. In the inset I we highlight how the branches of periodic orbits retract as e_* is increased. In Fig. 10(b) we show a magnification of the region II in Fig. 10(a) to highlight that the stable branches born at saddle-node bifurcations (SN) undergo period-doubling bifurcations (PD) for increasing ω, which we also see in Fig. 8(a). Figure 10(b) also shows how the unstable periodic orbits born at SN bifurcations disappear at grazing bifurcations (G). As mention above, these results are qualitatively in agreement with what is presented in [20]. The conclusion of this is that if the set of parameters are such that they lie to the left of the corresponding saddle-node bifurcation SN in Fig. 10(b) the long-term motion is stick and if they lie to the right of the period-doubling bifurcation PD the long-term motion is symmetric period-n ($n > 1$) or symmetric chaos. If the set of parameters are such the system is in-between SN and PD we can expect symmetric period-1 orbits in the long term.

5. Discussion

In this paper we introduced a framework for the numerical simulation of rigid-body systems with impacts and friction, specifically using the impact maps first derived in [28]. We present the framework for a general one-point rigid-body collision and show how the impact maps derived in [28] can be extended to allow for an impact between two unconstrained rigid bodies. Further we implemented the impact maps in a hybrid simulation environment in MATLAB, allowing for simulation of long-term dynamics of a planar rod where the two end points can impact an oscillating surface. For this purpose we introduced a framework that includes an ODE solver, system states and a transition diagram. This allowed us to reliably simulate the system in free flight, through impacts, in sticking and through complete chatter. For instance, the approach involved switching vector fields when the system is transitioning between stick and free flight motion, where the vector field for stick was found by calculating the normal force required to constrain the contact point to the surface.

In Table 1 together with Fig. 4 we presented a summary of what is needed to detect an event and what state transition the system will encounter. One of the shortcomings of our approach, and an area of future research, is

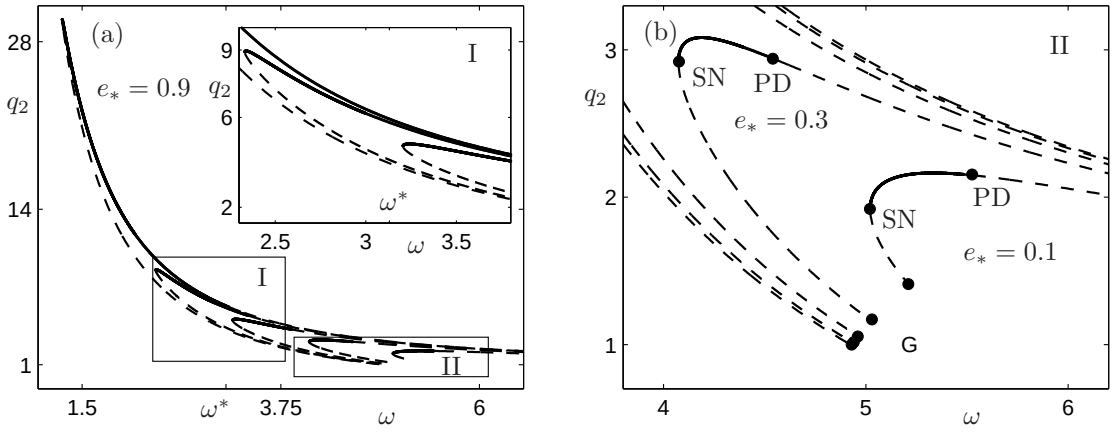

Figure 10: Bifurcation diagrams showing how the period-1 solution labeled p_1 in Fig. 8(a) varies with ω when $e_* = 0.9, 0.7, 0.5, 0.3$ and 0.1. Solid line represents the stable limit cycles and the dashed lines represent unstable limit cycles. In (a) all the branches are shown along with a magnification in panel I to further detail the structure. In (b) a magnification of panel II in (a) is shown. It highlights where the SN, PD and G bifurcations occur.

that we end a complete chattering sequence when the contact point velocity reaches an a priori defined velocity threshold V_{tol}, albeit small. This is in contrast to the method that was derived in [31] for impacts without friction, where at the end of a complete chatter sequence a jump in space and time is done to minimize local numerical errors. An improvement here would be to extrapolate through chatter sequences, using a similar approach as in [31], until the relative velocity is zero. Another related issue that is not fully resolved in this paper is in the limiting case whereby two impact events accumulate, and in our case where the rod angle θ approaches zero. In this case we, again, define a tolerance θ_{crit} a priori for when the transition from asymmetric to symmetric motion should occur. This was necessary to ensure robustness in the numerical scheme.

As mentioned above, we implemented this framework for the model example of a slender rod impacting a periodically forced surface. This example highlighted some of the phenomena present in impacting systems with friction, and in particular symmetric systems. The model example can, in some sense, be likened to the problem of machine rattle, whereby a machine element becomes detached and is free to undergo unconstrained mechanical vibration. For the rod system we examined the dynamics under variation of the frequency of surface oscillation ω. We showed that for high values of the restitution coefficient and low frequencies multiple periodic solutions coexist, however they do not survive an increase in ω, but instead chaotic regimes take over. Another aspect that was highlighted for low frequencies ω is how friction removes rotational energy so that mainly symmetric motions (impacts of both end points of the rod at the same time) persists. One of the main limitations of the symmetric rod system is that once it is in symmetric motion it can not get back to asymmetric motion. If an external torque was included or if the bar was not completely uniform then such a transition could occur and most likely make the system even more unpredictable. Although both generalisations would be possible to implement, they have not been considered for this work since the main goal was to introduce a framework for simulating long-term dynamics for a rigid-body system with impacts and friction and to highlight some interesting features that can be observed through long-term simulations.

The model example we chose to illustrate our techniques, albeit a simple geometry, was entirely unconstrained. Incorporating a more complex geometry, with more contact points, but with one or more constraints, would lead to a less complicated transition diagram than the one presented in Fig. 4. The advantage of the techniques presented in this paper is that they can be easily extended to and implemented for other mechanical systems, with relatively few contact points, where impacts and stick motions can occur. The implementation of our method would become increasingly difficult for an unconstrained system with more than two contact points, and it then may be necessary to consider a time-stepping scheme. However, it would then not be possible to perform the careful stability analysis techniques illustrated in this article. Further, the numerical scheme does not need to handle large number of events at one time and it is possible to deal with complete chatter sequences. The algorithm described here can also be exported directly to methods that locate periodic orbits and determine their stability using a shooting method, which is the only useful method to date that can be be used for periodic orbits with incomplete or complete chatter.

This article has opened up new research questions regarding numerical methods, as mentioned above, but also

the exact role friction has in dissipating rotational energy in general rattling objects. It may be possible to find a relationship between the energy removed due to friction and the energy introduced into the system through the periodic forcing. Such analysis may be a useful predictive tool for engineers working with unconstrained impacting systems with friction.

Acknowledgments

SB wishes to acknowledge the economic support from the National University of Ireland, Galway (NUI Galway) through a PhD scholarship in applied mathematics.

[1] Acary, V., Brogliato, B., 2007. Numerical methods for nonsmooth dynamical systems: Applications in Mechanics and Electronics. Vol. 35. Springer-Verlag.

[2] Adolfsson, J., Dankowicz, H., Nordmark, A., 2001. 3D passive walkers: Finding periodic gaits in the presence of discontinuities. Nonlinear Dynamics 24, 205–229.

[3] Alzate, R., di Bernardo, M., Montanaro, U., Santini, S., 2007. Experimental and numerical verification of bifurcations in cam-follower systems. Journal of Nonlinear Dynamics 50, 409–429.

[4] Alzate, R., Piiroinen, P. T., di Bernardo, M., 2012. From complete to incomplete chattering: a novel route to chaos in impacting cam-follower systems. International Journal of Bifurcation and Chaos 22 (5), 409–429.

[5] Barthel, E., 2008. Adhesive elastic contacts: JKR and more. Journal of Physics D: Applied Physics 41, 1–20.

[6] Brach, R. M., 1993. Classical planar impact theory and the tip impact of a slender rod. International Journal of Impact Engineering 13 (1), 21–33.

[7] Brach, R. M., 2007. Mechanical Impact Dynamics, Rigid Body Collisions. John Wiley & Sons, New York.

[8] Brogliato, B., 2007. Nonsmooth Mechanics. Springer-Verlag.

[9] Budd, C. J., Dux, F., 1994. Chattering and related behaviour in impact oscillators. Philosophical Transactions of the Royal Society of London A 347, 365–389.

[10] Budd, C. J., Piiroinen, P. T., 2006. Corner bifurcations in non-smoothly forced impact oscillators. Physica D 220, 127–145.

[11] Burns, S. J., Piiroinen, P. T., 2014. The complexity of a basic impact mapping for rigid bodies with impact and friction. Journal of Regular and Chaotic dynamics 19 (1), 20–36.

[12] Chillingworth, D., 2002. Discontinuity geometry for an impact oscillator. Dynamical Systems 17, 380–420.

[13] Dankowicz, H., Piiroinen, P. T., 2002. Exploiting discontinuities for stabilization of recurrent motions. Dynamical Systems 17, 317–342.

[14] di Bernardo, M., Budd, C. J., Champneys, A. R., Kowalcyzk, P., 2007. Bifurcation and Chaos in Piecewise Smooth Dynamical Systems- Theory and Applications. Springer-Verlag.

[15] di Bernardo, M., Budd, C. J., Champneys, A. R., Kowalczyk, P., 2008. Piecewise Smooth Dynamical Systems – Theory and Applications. Springer–Verlag, London UK.

[16] Fredriksson, M., Nordmark, A., 2005. Oblique frictional impact of a bar: Analysis and comparison of different impact laws. Nonlinear Dynamics 41, 361–383.

[17] Génot, F., Brogliato, B., 1999. New results on painlevé paradoxes. European Journal of Mechanics A/Solids 18, 653–677.

[18] Ghajari, M., Galvanetto, U., Iannucci, L., Willinger, R., 2011. Influence of the body on the response of the helmeted head during impact. International Journal of Crashworthiness 16 (3), 285–295.

[19] Goldsmith, W., 2001. Impact: The theory and physical behaviour of colliding solids. Dover Publications.

[20] Holmes, P. J., 1982. The dynamics of repeated impacts with a sinusoidally vibrating table. Journal of Sound and Vibration 84 (2), 173–189.

[21] Ivanov, A. P., 1992. Energetics of a collision with friction. Journal of Applied Mathematics and Mechanics 56, 527–534.

[22] Keogh, P. S., Cole, M. O. T., 2003. Rotor vibration with auxiliary bearing contact in magnetic bearing systems part 1: synchronous dynamics. Journal of Mechanical Engineering Science 217 (4), 377–392.

[23] Leine, R. I., Brogliato, B., Nijmeijer, H., 2002. Periodic motion and bifurcations induced by the painlevé paradox. European Journal of Mechanics A/Solids 21, 869–896.

[24] Leine, R. I., Nijmeijer, H., 2004. Dynamics and bifurcations of non-smooth mechanical systems. Lecture Notes in Applied And Compuational Mechanics 18.

[25] Leine, R. I., Van Campen, D. H., Glocker, C. H., 2003. Nonlinear dynamics and modelling of various wooden toys with impact and friction. Journal of Vibration and Control 9 (1-2).

[26] Mason, J., Homer, M., Wilson, R. E., 2007. Mathematical models of gear rattle in roots blower vacuum pumps. Journal of Sound and Vibration 308, 431–440.

[27] Nordmark, A., 2001. Existence of periodic orbits in grazing bifurcations of impacting mechanical oscillators. Nonlinearity 14, 1517–1542.

[28] Nordmark, A., Dankowicz, H., Champneys, A., 2009. Discontinuity-induced bifurcation in systems with impacts and friction: Discontinuities in the impact law. International Journal of Non-Linear Mechanics 44, 1011–1023.

[29] Nordmark, A., Dankowicz, H., Champneys, A., 2011. Friction-induced reverse chatter in rigid-body mechanisms with impacts. IMA Journal of Applied Mathematics 76, 85–119.

[30] Nordmark, A. B., 1991. Non-periodic motion caused by grazing incidence inimpact oscillators. Journal of Sound and Vibration 2, 279–297.

[31] Nordmark, A. B., Piiroinen, P. T., 2009. Simulation and stability analysis of impacting systems with complete chattering. Nonlinear Dynamics 58, 85–106.

[32] Osorio, G., D. B. M., Santini, S., 2005. Chattering and complex behaviour of a cam-follower system.

[33] Pfeiffer, F., Glocker, C., 2004. Multibody Dynamics with Unilateral Contacts. WILEY-VCH.

[34] Piiroinen, P. T., Dankowicz, H. J., 2005. Low-cost control of repetitive gait in passive bipedal walkers. International Journal of Bifurcation and Chaos 15 (6), 1959–1973.

[35] Piiroinen, P. T., Dankowicz, H. J., Nordmark, A. B., 2003. Breaking symmetries and constraints: Transitions from 2D to 3D in passive walkers. Multibody System Dynamics 10, 147–176.

[36] Piiroinen, P. T., Kuznetsov, Y. A., 2008. An event-driven method to simulate filippov systems with accurate computing of sliding motions. ACM Transactions on Mathematical Software 34 (3).

[37] Stronge, W. J., 1990. Rigid body collisions with friction. Mathematical and Physical Sciences 431 (1881), 169–181.

[38] Stronge, W. J., 2000. Impact Mechanics. Cambridge University Press.

[39] Wang, Y., Mason, M. T., 1992. Two-dimensional rigid-body collisions with friction. Journal of Apllied Mechanics 59, 635–642.

[40] Zhao, Z., Liu, C., Brogliato, B., 2009. Planar dynamics of a rigid body system with frictional impacts. II. qualitative analysis and numerical simulations. Proceedings of the Royal Society A 465, 2267–2292.